dynamic effects of ET-1. The spatial resolution is shown to be particular important because neighboring regions of interest are observed reacting differently to ET-1 simply depending on the surface vasculature that is present in the region. ET-1 can also cause concentration dependent changes in blood flow that could be used to mimic the different regions of an ischemia. In the future, this technique could be combined with multi-spectral reflectance imaging for results which would lead to an even better understanding of the hemodynamic effects of ET-1 which have yet to be fully explored.

REFERENCES

1. Adkins, D. L., A. C. Voorhies and T. A. Jones (2004). "Behavioral and neuroplastic effects of focal endothelin-1 induced sensorimotor cortex lesions." Neuroscience **128**(3): 473-86.
2. AHA (2006). Heart Disease and Stroke Statistics -- 2006 Update, American Heart Association, http://circ.ahajournals.org/cgi/content/short/113/6/e85.
3. Bonner, R., Nossal, R. (1981). "Model for laser Doppler measurements of blood flow in tissue." Appl Opt **20**: 2097-2107.
4. Briers, J. D. (1996). "Laser Doppler and time-varying speckle: a reconciliation." Optical Society of America **13**(2).
5. Briers, J. D. (2001). "Laser Doppler, speckle and related techniques for blood perfusion mapping and imaging." Physiol Meas **22**(4): R35-66.
6. Carmichael, S. T. (2005). "Rodent models of focal stroke: size, mechanism, and purpose." NeuroRx **2**(3): 396-409.
7. Cheng, H., Q. Luo, Q. Liu, et al. (2004). "Laser speckle imaging of blood flow in microcirculation." Phys Med Biol **49**(7): 1347-57.
8. Cheng, Y. D., L. Al-Khoury and J. A. Zivin (2004). "Neuroprotection for ischemic stroke: two decades of success and failure." NeuroRx **1**(1): 36-45.
9. Dunn, A. K., H. Bolay, M. A. Moskowitz, et al. (2001). "Dynamic imaging of cerebral blood flow using laser speckle." J Cereb Blood Flow Metab **21**(3): 195-201.
10. Fercher, A., Briers, J. (1981). "Flow visualization by means of single exposure speckle photography." Opt Commun **37**: 326-329.
11. Fuxe, K. (1997). "Endothelin-1 induced lesions of the fronto-parietal cortex of the rat." NeuroReport **8**: 2623-2629.
12. Fuxe, K., N. Kurosawa, A. Cintra, et al. (1992). "Involvement of local ischemia in endothelin-1 induced lesions of the neostriatum of the anaesthetized rat." Exp Brain Res **88**(1): 131-9.
13. Gilmour, G., S. D. Iversen, M. F. O'Neill, et al. (2004). "The effects of intracortical endothelin-1 injections on skilled forelimb use: implications for modelling recovery of function after stroke." Behav Brain Res **150**(1-2): 171-83.
14. Goodman, J. (1965). "Some effects of target-inducec scintillation on optical radar performance." Proc IEEE **53**: 1688-1700.
15. Koizumi J, Y. Y., Nakazawa T, Ooneda G (1986). "Experimental studies of ischemic brain edema. I. A new experimental model of cerebral embolism in which recirculation can be introduced into the ischemic area." Jpn J Stroke **8**: 108.
16. Sharkey, J., I. M. Ritchie and P. A. Kelly (1993). "Perivascular microapplication of endothelin-1: a new model of focal cerebral ischaemia in the rat." J Cereb Blood Flow Metab **13**(5): 865-71.
17. Windle, V., A. Szymanska, S. Granter-Button, et al. (2006). "An analysis of four different methods of producing focal cerebral ischemia with endothelin-1 in the rat." Exp Neurol **201**(2): 324-34.

Characterization of Cell Samples from Measurements of Spectroscopic Scattering Phase-Dispersion*

Shellee D. Dyer[a♦], Lara K. Street[a], Shelley M. Etzel[a], Tasshi Dennis[a], Andrew Dienstfrey[b], Vadim Tsvankin[c], and Wei Tan[c]

[a]NIST, Optoelectronics Division, Mailstop 815.03, 325 Broadway, Boulder, CO 80305

[b]NIST, Mathematical and Computational Sciences Division, 325 Broadway, Boulder, CO 80305

[c]University of Colorado, Department of Mechanical Engineering, Boulder, CO 80309

ABSTRACT

We present spectroscopic swept-source optical coherence tomography (OCT) measurements of the phase-dispersion of cell samples. We have previously demonstrated that the phase of the scattered field is, in general, independent of the intensity, and both must be measured for a complete characterization of the sample. In this paper, we show that, in addition to providing a measurement of the size of the cell nuclei, the phase spectrum provides a very sensitive indication of the separations between the cells. Epithelial cancers are characterized by many factors, including enlarged nuclei and a significant loss in the architectural orientation of the cells. Therefore, an *in vivo* diagnostic tool that analyzes multiple properties of the sample instead of focusing on cellular nuclei sizes alone could provide a better assessment of tissue health. We show that the phase spectrum of the scattered light appears to be more sensitive to cell spacing than the intensity spectrum. It is possible to determine simultaneously the cell nuclei sizes from the intensity spectrum and the nuclei spacing from the phase spectrum. We measure cell monolayer samples with high and low cell density and compare measured results with histograms of the cell separations calculated from microscope images of the samples. We show qualitative agreement between the predicted histograms and the interferometric results.

Keywords: Dispersion; Interferometry; Optical Coherence Tomography; Phase Measurement; Scattering Measurements.

1. INTRODUCTION

The combination of optical coherence tomography (OCT) with light scattering spectroscopy (LSS) offers a powerful tool for tissue diagnostics, including the potential for *in vivo* detection of cancer and its precursors [1]. Much of the research in this field has focused on determining the size and/or refractive index of the cellular nuclei, as enlarged nuclei are often described as one potential indicator of cancerous tissue. This is typically accomplished by measuring the intensity of the light scattered from the sample as a function of angle [2] or wavelength [3]. The size and/or refractive index of the scatterer is then determined through a least-squares curve fitting to a database of scattering curves [4], or, assuming a first-order Born approximation [5], the optical path length of the scatterer can be determined from a Fourier transform of the scattering data [6]. However, enlarged nuclei are not the only factor that pathologists consider when examining a tissue sample. If we focus specifically on epithelial cancers, which account for over 70 % of all cancers, the earliest cancer precursor is dysplasia, which is characterized not only by abnormally large and hyperchromatic nuclei, but also by a significant loss in the intercellular architectural orientation [7]. Therefore, an *in vivo* measurement of both the size of the nuclei and the spacing between the nuclei would provide a richer assessment of the tissue health than a measurement of nuclei size alone. Recent research has accomplished this by identifying both short- and long-range correlations in the Fourier transform of the magnitude of the scattering signal as a function of angle [8-9]. In this paper we will demonstrate that the phase of the scattered signal appears to be much more sensitive to the spacing between nuclei than is the magnitude of that same signal. In previous work, we demonstrated that the scattering process is, in general, non-minimum phase, and therefore that the phase of the scattered light provides information that is not available if the magnitude alone is measured [10]. In this paper, we show that measuring both magnitude and phase provides a

♦ sdyer@boulder.nist.gov, phone 303.497.7463, fax 303.497.7621

Biomedical Applications of Light Scattering, edited by Adam Wax, Vadim Backman,
Proc. of SPIE Vol. 6446, 64460V, (2007) · 1605-7422/07/$18 · doi: 10.1117/12.701239

more complete assessment of the sample, and that measuring the full complex scattered field may provide an exceptionally sensitive indication of both nuclei size and spacing.

In general, any scattering sample can be modeled with a complex transfer function $H(\omega)=\rho(\omega)\exp(i\phi(\omega))$, where and ω is the angular frequency, $\rho(\omega)$ represents the magnitude of the scattered light, and $\phi(\omega)$ the phase. The optical phase has two components: material dispersion, which arises from the wavelength dependence of the refractive index, and scattering dispersion, which results from the wavelength dependence of the Mie scattering that typically occurs in tissue. For samples such as tissue, which exhibit strong scattering, the material dispersion is likely negligible compared with the scattering dispersion, and we treat our measurements as scattering dispersion alone. Since measurements of optical phase are usually relative rather than absolute, phase is often described by the relative group delay (RGD), which is defined as $d\phi/d\omega$, where ϕ is the phase of the electric field.

2. EXPERIMENTAL SCHEME

Our spectral domain OCT system is shown in Fig. 1. The system consists of two interferometers: a fiber-optic Michelson reference interferometer to track the wavelength of the tunable laser as it is swept, and a Fabry-Perot type measurement interferometer. In this case, our samples consist of monolayers of cells on one surface of a microscope slide; some slides also have a cover slip over the cells to protect them from environmental influence. Our measurement interference signal is created from interference of the light scattered from the cell monolayer with the light reflected from the other surface of the microscope slide. The sample was illuminated with a nominally collimated beam with a diameter of 1.3 mm. The signal from the reference interferometer is sent to a zero crossing circuit, which is used to trigger sampling of the measurement interferometer signal.

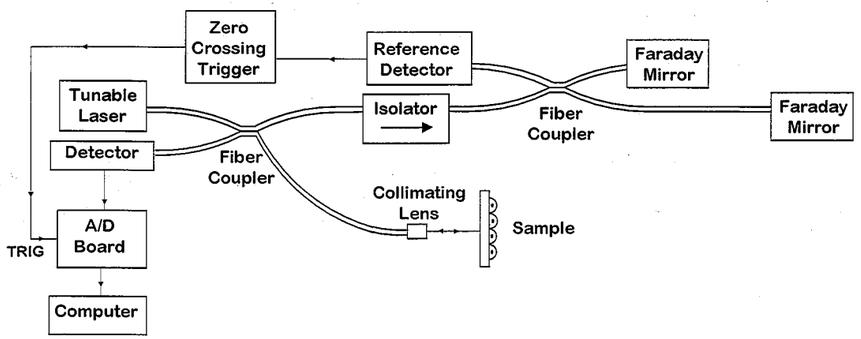

Fig. 1. Diagram of the OCT system used for scattering measurements. It consists of two interferometers: a fiber-optic Michelson reference interferometer to track the wavelength of the laser as it is swept, and a Fabry-Perot measurement interferometer, in which the interference is created by the front and rear surfaces of the microscope slide.

Starting with the interferogram as a function of frequency, we perform an inverse Fourier transform to obtain the time-domain interferogram. We then apply a Hamming window to the time-domain signal to remove the DC and autocorrelation terms and one of the complex conjugate impulse response terms. We then calculate the RGD from the following formula [11]:

$$t_g(\omega)\equiv\frac{d\phi(\omega)}{d\omega}=\mathrm{Re}\left\{\frac{FT(\tau I(\tau))}{FT(I(\tau))}\right\}, \tag{1}$$

where t_g is the relative group delay, ϕ is the phase of the electric field, τ is the delay time, $I(\tau)$ is the windowed time-domain interferogram, and Re represents the real part of the function. The wavelength resolution of the RGD result is inversely proportional to the width of the window. The optimal window width is a tradeoff between wavelength resolution and RGD resolution; larger windows give better wavelength resolution, but include more noise, thereby degrading the RGD resolution.

For comparison, we also calculated the magnitude of the scattering spectrum as follows:

$$\rho_{um}(\omega)=\left|FT(I(\tau))\right|, \tag{2}$$

where ρ_{um} is the unnormalized magnitude of the scattering spectrum. The scattering spectrum requires a normalization to remove the background intensity created by the changes in the laser's power as it is swept. Therefore, we also measured a blank microscope slide and used its magnitude spectrum (ρ_{ref}) to calculate $\rho(\omega)$ as follows:

$$\rho(\omega)=\frac{\rho_{um}(\omega)}{\rho_{ref}(\omega)}. \tag{3}$$

In this analysis, we use a first-order Born approximation, which assumes weak scattering, as could generally be expected in biological tissue. We can then determine the approximate size of our scatterers from an inverse Fourier transform of $\rho(\omega)$ or $t_g(\omega)$ as follows: the spectral density of the scattered magnitude is given by

$$\Gamma_\rho=\left|FT^{-1}(\rho(\omega))\right|, \tag{4}$$

while the spectral density of the group delay is calculated from

$$\Gamma_{t_g}=\left|FT^{-1}(t_g(\omega))\right|. \tag{5}$$

In both cases, we determine the size of the scatterer from the first peak in the spectral density. The group delay is described as relative group delay because it includes an arbitrary additive constant that is determined by the choice of the position of t = 0 in the time-domain signal. For this reason, we can subtract the mean value of the RGD before calculating the Fourier transform of the RGD to obtain the RGD spectral density, effectively eliminating the large DC spike that sometimes plagues the calculation of the spectral density of the scattered intensity [6]. We also subtracted the mean value of the magnitude function $\rho(\omega)$ to avoid a DC spike in the Γ_ρ function.

3. PREPARATION OF CELL MONOLAYER SAMPLES

Experiments were conducted on a monolayer of rat vascular endothelial cells (VECs). The cells (provided by the University of Colorado Health Sciences Center) were grown in 75 cm^2 tissue culture flasks (tissue-culture treated, with filtered screw caps), by use of 10 mL of Dulbecco's Modified Eagle's Medium* as a growth medium, supplemented with 10 % fetal bovine serum and 1 % penicillin-streptomycin solution (10,000 I.U. penicillin, 10 mg streptomycin per mL in 0.9 % NaCl). Cells were incubated at 37 °C in a humidified atmosphere of 5 % CO_2 in air.

For these experiments, cells were seeded on a glass slide at 300,000 U.I./mL. This was done by removing media and incubating with 2.5 mL Trypsin-EDTA solution (0.05 % Trypsin, 0.53mM EDTAx4Na). Subsequently, 5 mL of growth medium was added and cells were transferred to a 15 mL centrifuge tube and centrifuged at 1500 RPM for 10 minutes, yielding a cell pellet. Growth medium and Trypsin-EDTA were removed, and cells were resuspended in fresh growth

* Product names are included for completeness of the technical description, but this does not constitute an endorsement of any particular company's product. Other manufacturers may offer products that work as well or better.

medium. A hemocytometer was used to seed at the desired cell density. Twenty-four hours following seeding, cells were treated with Hematoxylin for 20 minutes at room temperature, rinsed with phosphate buffer solution (PBS), and then fixed for 10 minutes with 3.7 % formaldehyde in PBS. Samples were then dehydrated by use of a graded ethanol series and mounted with Histomount. Although the cells were seeded to achieve a nominally uniform density across the surface of the microscope slide, when we examined the slide under a microscope, we found that there were fairly significant variations in the cell density. In small regions of the slide (on the order of 4 mm^2), the cell density was approximately uniform, but over large distances (greater than 20 mm), significant variations in density were observed. This could be attributed to a number of factors, including regional variations in growth factors, heterogeneities of the glass surface, or (most likely) seeding that wasn't perfectly uniform across the slide.

4. MEASUREMENT RESULTS

We first verified our measurement capabilities by measuring monolayers of polystyrene spheres deposited on the surface of microscope slides and comparing our measurement results with the sphere manufacturers' size specifications. These measurements are described in detail in [12]. In our experiments with cell monolayers, we started with the goal of determining the size of cells' nuclei. We measured the samples and calculated the group delay as described above and then calculated the size of the nuclei from a Fourier transform of the group delay signal. In this experiment, we were illuminating a large number (more than 100) of nuclei simultaneously, and the cells are highly nonuniform, so we expected to obtain an average value for the size of the nuclei. For comparison, we calculated the average size of the nuclei from a microscope image of the samples using a commercial image processing software program. Although the results agreed reasonably well, this comparison is not optimal. First, the resolution of the interferometric measurement is limited by the bandwidth of the swept laser. In our case, our laser sweeps over a 117 nm bandwidth, and we found that the extreme long and short wavelengths of this range must be truncated because of uncertainties created by the laser as it begins and ends a sweep. We truncated the first and last 7 % of the sweep range, giving a net sizing resolution of 6 μm, assuming a refractive index of 1.4. Given the fact that healthy nuclei typically have sizes from 4-7 μm, the resolution of 6 μm is barely adequate for this assessment. Another significant problem with this comparison is the cell monolayer and its nuclei, which are not truly spherical, will be further distorted by the microscope slide as shown in Fig. 2 [6]. In this figure we note that, in general, we can expect that the nuclei will be ellipsoidal in shape, with some distortion in the shape created by the microscope slide. Our microscope measures the transverse diameters (x_{t1} and x_{t2}) of the nuclei, while the interferometric measurement likely measures the diameter that is longitudinal to the incident beam (x_l).

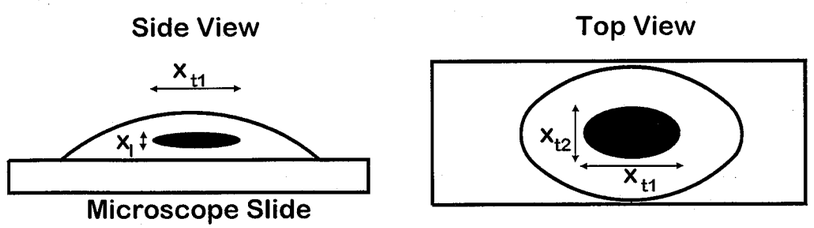

Fig. 2. Diagram of a cell on the surface of a microscope slide. The nucleus is ellipsoidal, with some distortion of its shape resulting from interactions of the cell with the microscope slide.

One interesting result from the cell monolayer measurements came from a comparison of measurements performed on different regions of the monolayer. We marked several 4 mm^2 target areas on the surface of the microscope slide and aligned our interferometric measurement system to center the beam on the marked area. From a microscope image of the target regions that was approximately centered on the 4 mm^2 targets, we identified two areas with markedly distinct

cell densities, as shown in Fig. 3. Both images are at 10 X magnification; therefore, the differences in cell density are likely the result of nonuniform seeding or one of the other factors discussed above. Each of the microscope images cover an area of 650 μm by 880 μm, compared with the Gaussian beam of the interferometric measurement, which has a diameter of 1.3 mm.

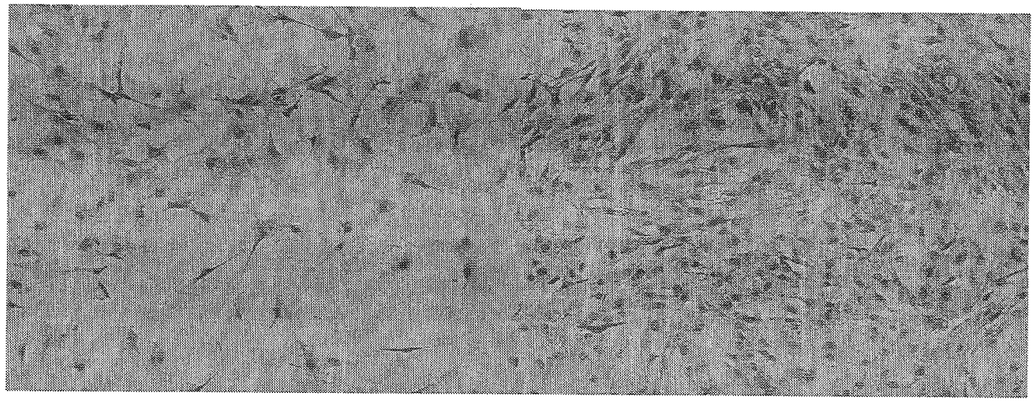

(a) (b)

Fig. 3. Micrograph images of two distinct areas of a VEC monolayer on a microscope slide. Both images were taken at 10 X magnification. (a) Region of low cell density. (b) Region of high cell density. The surface of the microscope slide was not pristine, which likely created the streaks observed in the images.

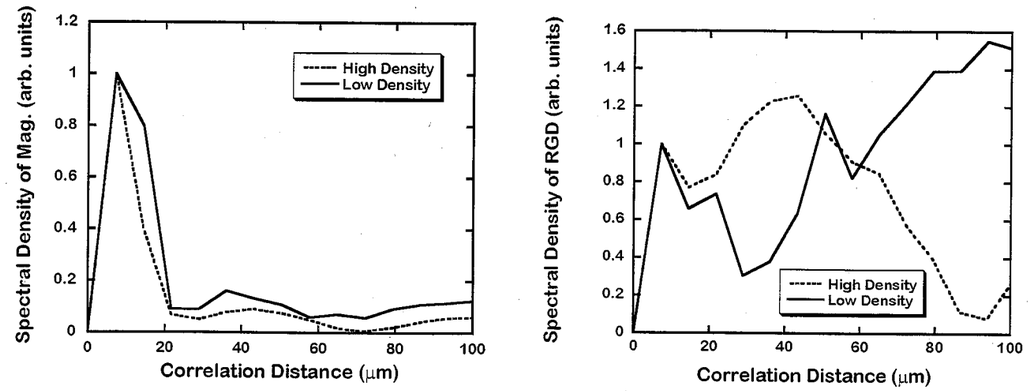

(a) (b)

Fig. 4. Comparison of the Fourier transform of the scattered intensity spectrum and the Fourier transform of the RGD spectrum calculated from measurements of the high and low density regions of the VEC sample shown in Fig. 3. In (a) we show the spectral density of the scattering magnitude, while in (b) we show the spectral density of the RGD. In all cases we see a peak at a correlation distance of 6 μm, which likely results from the scattering from the cells' nuclei. However, the spectral density of the RGD measurement shows a clear difference at larger correlation distances, likely resulting from the difference in density between the two samples.

We measured the two areas of the VEC monolayer shown in Fig. 3 and calculated the RGD and magnitude spectra as described above. In this case, we were interested in measuring the long-range correlations of the cell monolayer; therefore, we used a broader window on the time-domain signal than we would typically use to calculate RGD. We applied a Hamming window of length 2.8 ps (which, assuming a refractive index of 1.4, corresponds to a physical distance of 300 μm) to the time domain signal before calculating the group delay. In Fig. 4 we show the spectral density of the RGD (Γ_{tg}) as well as the spectral density of the magnitude spectrum (Γ_p) from measurements of the high and low density regions of the VEC slide (from Fig. 3), both calculated as described in Eqs. 1-5 above.

From Fig. 4, we see that, in both the regions of high and low cell density, both the spectral density of the magnitude spectrum and the spectral density of the RGD have clear peaks at a correlation distance of 6 μm. This is a typical size that one could expect healthy cell nuclei to exhibit, and therefore we believe that this peak indicates scattering from the nuclei. When we examine the signals of Fig. 4(b) at correlation distances larger than 6 μm, some clear difference emerge. We see a significant difference between the high- and low-density samples at the larger correlation distances, and we note that the intensity spectral density in 4(a) does not exhibit as large a difference between low- and high-density cell samples. We believe that these higher-order correlations could be used to calculate the spacing between the nuclei in the sample. The scattering process is, in general, non-minimum phase, and therefore it is not surprising that there is a clear difference between the scattering intensity spectral density and RGD spectral density. This indicates that, from a single measurement of a tissue sample, the scattered intensity could be used to determine the size of the nuclei, while the RGD could be used to distinguish between high- and low-density cell architectures.

5. MODELING THE SCATTERING PROCESS

For simplicity, we model the ellipsoidal nuclei as spheres. Assuming plane-wave illumination, Mie derived an expression for the scattering from a single spherical object [13] that yields an approximately sinusoidal signal for both the magnitude and phase of the scattered spectrum, with the periodicity of the signal determined by the size of the scatterer.

To model the case of multiple scatterers, we assume fixed illumination and scattering directions ($\hat{k}_i$ and $\hat{k}_s$) and a single polarization defined with respect to the resulting scattering plane. For the nth scatterer (in our case, the nucleus of the nth cell) the scattering matrix relates the incident plane wave field to the scattered radiation, $E_{s,n} = S_n\left(\hat{k}_s, \hat{k}_i, \underline{x}_n\right) E_{i,n}$ where the vector $\underline{x}_n$ denotes the center of the nth scatterer. Assuming single scattering and that, to first order, the cell nuclei scatter identically, then the scattered field for an ensemble of cells may be simplified by use of the translation theory for S:

$$S_{tot} = \sum S_n\left(\hat{k}_s, \hat{k}_i, \underline{x}_n\right) = S_0(\hat{k}_s, \hat{k}_i, \underline{O})\left[1 + \sum_{\underline{x}_n \neq 0} \exp\left(i\left(\underline{k}_i - \underline{k}_s\right) \cdot \underline{x}_n\right)\right] \tag{6}$$

Thus we see that the phase of the scattered field is determined by two parts: the phase response of the isolated scatterer field S_0 as well as the coherent scattering effects due to translation. In an ideal back-scattering geometry, $k_s = -k_i$. Furthermore, if the cell nuclei are translated in a plane orthogonal to this direction, then the exponential term sums coherently as $\exp\left(i\left(k_i - k_s\right) \cdot x_n\right) = \exp\left(i2k_i \cdot x_n\right) = \exp(0) = 1$. Our experiment approximates this ideal case, but the incident and scattered vectors are not perfectly parallel, and the translation vectors representing the cell locations are not perfectly orthogonal to the incident and scattered vectors. The conclusion is that there is an (as yet undetermined) scale factor that accounts for these alignments, resulting in a nontrivial projection of nuclei translations and a corresponding effect in the scattered phase. Although our cell samples are nominally aligned perpendicular to the incident beam in our measurements, we were still able to observe a signal representing the separation between the cells, due to the imperfections of our measurement: the distance between the nuclei and the microscope slide may be different for each cell, the microscope slide may not be perfectly perpendicular to the incident beam, and the incident beam is not a pure plane wave.

To compare our experimental results with predicted values, we started with the cell micrographs shown in Fig. 3. For each micrograph, we used image-processing techniques to find the approximate center of each nuclei (402 nuclei in the case of the high-density image, 97 in the low-density image). We then identified the nucleus closest to the center of the image, and calculated the distances from that nucleus to all other nuclei in the image. We then created a histogram of those distances, which we expect should correspond to the peaks at correlation distances larger than 6 μm in Fig. 4(b). Therefore, we performed a curve fit of the histogram to the RGD spectral density plot, using both the peak spectral density and the correlation distance of the RGD spectral density as free parameters. The amplitude of the spectral density of the RGD was only measured as a relative value and was therefore treated as a free parameter. The free scale factor in the correlation distance arises from the systematic effects described above in the context of Eq. (6): the slide may not be perfectly normal to the incident and scattered beams, and the incident beam is not a true plane wave. However, it is important to note that the same correlation-distance scale factor was applied to both histograms. The comparisons of the RGD spectral density with the histograms calculated from the micrographs are shown in Fig. 5 for both the high and low cell density cases.

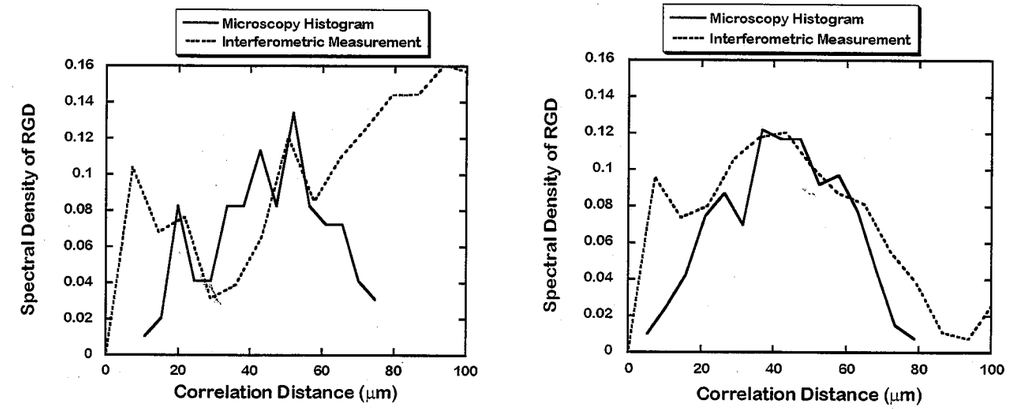

(a) (b)

Fig. 5. Comparison of the RGD spectral density with a histogram plot of the distances from the "central nucleus" to all other nuclei calculated from a microscopic image of each sample. (a) Low cell density. (b) High cell density.

One limitation of the above comparison is that the histogram was calculated from an image that covered an area of 0.6 mm^2, compared to the 1.3 mm^2 area sampled by the Gaussian beam of the interferometric measurement. However, given the large number of cells present in the micrograph images of Fig. 3, we expect that the histograms of Fig. 5 are a reasonable approximation to the cell distributions present in the interferometric measurement. However, as is true for any statistical calculation, more data would give better results. Although we made some measurements with a smaller collimated beam, we found our best results were achieved with the 1.3 mm diameter beam, because the measured data represented the average over many cells. Additionally, from Fig. 5, we see a better agreement between the histogram and the interferometric data for the case of the high cell density, in which the histogram was calculated from the relative positions of 402 cells, than we do in the case of the low cell density, in which the histogram was calculated from only 97 cells.

6. CONCLUSIONS

In this paper, we have demonstrated that the phase (group delay) measured from a cell monolayer is strongly affected by the spacing between the cells. In previous work, we have demonstrated that the scattering process is, in general, non-

minimum phase; thus we expect that the phase will provide information that is not available to a measurement of magnitude alone. An experimental scheme that includes measurements of both magnitude and phase will provide more information than is available to a measurement of the scattered intensity alone. For example, we have demonstrated that group delay appears to be more sensitive than the intensity spectrum to the spacing between the cells. Hence, from a single interferometric measurement, one could use the scattered intensity spectrum to determine the average size of the nuclei scatterers in the sample, and use the phase spectrum to determine the cell spacing.

Examination of *ex vivo* tissue by a pathologist is the current "gold standard" for cancer screening, thus it is expected that the most accurate *in vivo* cancer screening techniques will examine tissue by use of the same criteria that pathologists use. For epithelial cancers, these criteria include increased nuclear-cytoplasmic ratio, a loss of architectural orientation, pleomorphism, and hyperchromaticity. The measurement of the full (complex) scattering function $H(\omega)$ can be used to determine both nucleus size and cell spacing, providing more information than a measurement of the magnitude alone. Therefore we expect that this measurement would improve the accuracy of cancer screening techniques. Although our measurements were performed on a cell monolayer where a two-dimensional geometry is enforced by presence of the microscope slide, these measurements may be even more significant for *in vivo* tissue where a less ordered three-dimensional structure is expected.

REFERENCES

1. U. Morgner, W. Drexler, F.X. Kärtner, X.D. Li, E.P. Ippen, and J.G. Fujimoto, "Spectroscopic optical coherence tomography," *Opt. Lett.* **25**, 111-113 (2000).
2. A. Wax, C. Yang, R.R. Dasari, and M.S. Feld, "Measurement of angular distributions by use of low-coherence interferometry for light-scattering spectroscopy," *Opt. Lett.* **26**, 322-324 (2001).
3. A. Wax, C. Yang, and J.A. Izatt, "Fourier-domain low-coherence interferometry for light scattering spectroscopy," *Opt. Lett.* **28**, 1230-1232 (2003).
4. J.W. Pyhtila, R.N. Graf, and A. Wax, "Determining nuclear morphology using an improved angle-resolved low coherence interferometry system," *Opt. Express* **11**, 3473-3484 (2003).
5. L. Mandel and E. Wolf, *Optical Coherence and Quantum Optics*, Cambridge University Press, New York, 1995, pp. 403-414.
6. R. N. Graf and A. Wax, "Nuclear morphology measurements using Fourier domain low coherence interferometry," *Opt. Express* **13**, 4693-4698 (2005).
7. R.S. Cotran, V. Kumar, and T. Collins, *Robbins Pathologic Basis of Disease*, 6th Edition, W.B Saunders Company, Philadelphia, 1999, Chap. 8.
8. A. Wax, C. Yang, V. Backman, K. Badizadegan, C.W. Boone, R.R. Dasari, and M.S. Feld, "Cellular organization and substructure measured using angle-resolved low-coherence interferometry," *Biophysical J.*, **82**, 2256-2264 (2002).
9. J.W. Pyhtila, H. Ma, A.J. Simnick, A. Chilkoti, and A. Wax, "Analysis of long range correlations due to coherent light scattering from *in vitro* cell arrays using angle-resolved low coherence interferometry," *J. Biomedical Optics* **11**, 034022 (2006).
10. S.D. Dyer, T. Dennis, L.K. Street, S.M Etzel, T.A. Germer, and A. Dienstfrey, "Spectroscopic phase-dispersion optical coherence tomography measurements of scattering phantoms," *Opt. Express* **14**, 8138-8153 (2006).
11. V. Laude, "Noise analysis of the measurement of group delay in Fourier white-light interferometric cross correlation," *J. Opt. Soc. Am. B*, **19**(5), 1001-1008 (2002).
12. T. Dennis, S.D. Dyer, and A. Dienstfrey, "Phase-dispersion light scattering for quantitative size-imaging of spherical scatterers," accepted for publication in SPIE BiOS (2007).
13. G. Mie, "Beitrage zur Optik trüber Medien speziell kolloidaler Metallösungen," *Ann. Phys.* **25**, 377–445 (1908).

Side scatter light for micro-size differentiation and cellular analysis

Xuan-Tao Su*[a], Wojciech Rozmus[a], Clarence Capjack[b], and Christopher Backhouse[b]

[a]Department of Physics, University of Alberta, Edmonton, T6G 2G7, Canada
[b]Department of Electrical & Computer Engineering, University of Alberta, Edmonton, T6G 2V4, Canada

ABSTRACT

High resolution 2D side scatter patterns from polystyrene beads were obtained by using an integrated microfluidic waveguide cytometer. A He-Ne laser beam was prism-coupled into a microfluidic chip, and waveguide modes were excited to illuminate a single scatterer. While immobilizing a single scatterer on chip in the observation window area, high resolution 2D scatter patterns were obtained by using a CCD array located beneath the microchip. This cytometer is sensitive to variations in both the refractive index and the size of a single scatterer. Fourier transforms of Mie simulation results from a single scatterer show that forward scattered light at large angles is optimal for micro-size differentiation. While side scatter light was reported to contain rich information about organelles in a single cell, we show here that side scatter light can be used to perform fast micro-size differentiation and cellular analysis. A cross section scan of the experimental scatter pattern gives an oscillation distribution of the scattered intensity. This oscillation has a frequency that is typical for a given micro-size scatterer. A Fourier method for quick micro-size differentiation is reported, based on the comparisons between the Mie simulations and the experimental results. Finite-difference time-domain (FDTD) simulations of single white blood cells in the waveguide cytometer are studied, which allows extraction of micro-structural and nano-structural information from single cells.

Keywords: Light scattering, single cell, side scatter, microfluidics, waveguide, cytometer, FDTD

1. INTRODUCTION

The analysis of light scattering from single biological cells has great applications in clinics, such as precancerous cell detection.[1] When polarized laser light illuminates a cell, light is scattered in all directions. The spatial distribution of the scattered light is not random, and is reported that different scatter angular ranges contain information about different cell components. Forward scattering (0.5^0~5^0 in polar angle, where the incident wave vector is assumed to be along the $+z$ direction) provides information about the size of the cell plasma. The nucleus, the largest organelle in a cell, mainly contributes to scattered light at larger angles (5^0~30^0 in polar angle).[2,3] Numerous studies have indicated that nanoscale structures such as mitochondria in a cell play important role in the observed side scatter (50^0~130^0 in polar angle).[3~5]

The challenge of micro-alignment of the scatterer and the detector in the bulk optics systems, and the lack of an effective method of trapping or otherwise immobilizing the scatterer in the microfluidic flow, make it difficult to address side scatter in single cell light scattering measurements. However it is the side scatter that contains most of the information about the mitochondria in a single cell. Residues left in the channel and leakages are the problems that are encountered with most microchip fabrication methods such as soft lithography based[6] or epoxy based[7] microchip fabrications. Because the side scattering from a single biological cell is weak, a clean channel will help to lower the background scattering.

Flow cytometry has been widely used for cellular analysis to obtain size or refractive index information of biological cells by using light scattering measurements. The commonly used method to extract this information is by matching the experimental scatter spectra with theoretical simulation results. The Fourier method for simultaneous determination of the size and refractive index information of cells can potentially be useful in the real time characterization of cell

*xtsu@phys.ualberta.ca; phone 1 780 492 6432; fax 1 780 492 0714

Biomedical Applications of Light Scattering, edited by Adam Wax, Vadim Backman,
Proc. of SPIE Vol. 6446, 64460W, (2007) · 1605-7422/07/$18 · doi: 10.1117/12.701549